A Utility-Scale Flywheel Energy Storage System with a Shaftless, Hubless, High-Strength Steel Rotor

Xiaojun Li, *Student Member, IEEE*, Bahareh Anvari, *Member, IEEE*, Alan Palazzolo, Zhiyang Wang, and Hamid Toliyat, *Fellow, IEEE*

***Abstract*—Energy storage is crucial for both smart grids and renewable energy sources such as wind or solar, which are intermittent in nature. Compared to electrochemical batteries, flywheel energy storage systems (ESSs) offer many unique benefits such as low environmental impact, high power quality, and larger life cycles. This paper presents a novel utility-scale flywheel ESS that features a shaftless, hubless flywheel. The unique shaftless design gives it the potential of doubled energy density and a compact form factor. Its energy and power capacities are 100 kWh and 100 kW, respectively. The flywheel is made of high-strength steel, which makes it much easier to manufacture, assemble, and recycle. Steels also cost much less than composite materials. Design and analysis of the shaftless flywheel are presented first. In addition, the system incorporates a new combination active magnetic bearing. Its working principle and levitation control for the flywheel are discussed. The design of an integrated coreless permanent-magnet (PM) motor/generator for the flywheel is given as well. Initial test results show that the magnetic bearing provides stable levitation for the 5443-kg flywheel with small current consumption.**

***Index Terms*—Energy storage, flywheel, frequency regulation, magnetic bearing, magnetic levitation, permanent-magnet (PM) machine, renewable energy.**

I. Introduction

THE Paris Climate Pact, which will take effect in 2020, has called on nations worldwide to “hold the increase in average global temperature to well below 2 °C above the pre-industry level” and pursue the goal of 1.5 °C above the pre-industry level. To achieve this, it is necessary to reduce greenhouse gas emissions generated by burning fossil fuel in power plants. However, rapid economic development is driving up electricity consumption. Many places in the world are still suffering from electrical shortages. Efficiently storing and distributing energy is becoming a critical challenge but also an opportunity. Energy storage systems (ESSs) can play an essential role for power grids in many aspects [1]. First, ESSs provide frequency regulations and voltage sag compensations to improve the power quality of the grid. Second, they can be utilized as bridges in providing a short duration power supply for critical or high-power-demanding applications [2]. A flywheel ESS (FESS) converts electrical energy and stores it as kinetic energy through a bidirectional power converter, which also allows the stored energy to be discharged back to electrical grid [3]. FESSs are usually supported by active magnetic bearing (AMB) systems to avoid any friction loss or wear by conventional bearings so that they can store energy at high efficiency over an extended period. When compared to electrochemical ESSs such as Li-on batteries, FESSs are ideal solutions to utility-scale ESS due to their high power rating and quality, superior depth of discharge, and number of lifetime charge cycles [3]. In addition, they have a very limited environmental impact. It is worth mentioning that apart from power grid regulations, FESSs have also been designed as an integral part of renewable energies such as wind and solar farms to improve their efficiencies [3]–[5].

Major efforts are made in building innovative FESSs. They can generally be summarized in the following areas: design and optimization of the flywheel itself to achieve higher optional speed [6] or design of innovative magnetic bearings and motor/generator systems [7], [8]. Arvin and Bakis [9] have proposed a concept design of a flywheel made of multiple rims, press-fit, filament-wound composite materials. The optimization uses simulated annealing algorithm and yields a specific energy of 40–50 kWh/kg. Sung *et al.* [10] developed a 300 Wh flywheel supported by two superconducting magnetic bearings. The superconducting magnetic bearing does not need active control and was capable of achieving 20 000 r/min spin speed. Beacon Power Corporation commissioned a frequency regulation power plant with flywheels made of carbon fibers. A single unit costs \$260 k (estimated) and is capable of 25 kWh. The project budget is over \$40 million. It is capable of 20 MW

Manuscript received March 31, 2017; revised August 22, 2017; accepted September 28, 2017. Date of publication November 13, 2017; date of current version April 2, 2018. This work was supported in part by the Texas A&M Energy Institute under Grant 292. *(Corresponding author: Xiaojun Li.)*

X. Li is with the Department of Mechanical Engineering, Texas A&M University, College Station, TX 77840 USA, and also with the Motion Control Group, Rockwell Automation, Eden Prairie, MN 55344 USA (e-mail: tonylee2016@gmail.com).

B. Anvari and H. Toliyat are with the Department of Electrical Engineering, Texas A&M University, College Station, TX 77840 USA (e-mail: anva28@tamu.edu; toliyat@tamu.edu).

A. Palazzolo is with the Department of Mechanical Engineering, Texas A&M University, College Station, TX 77840 USA (e-mail: apalazzolo@tamu.edu).

Z. Wang is with Calnetix Technology, Cerritos, CA 90703 USA (e-mail: hitwzy@gmail.com).

Color versions of one or more of the figures in this paper are available online at http://ieeexplore.ieee.org.

Digital Object Identifier 10.1109/TIE.2017.2772205

0278-0046 © 2017 IEEE. Personal use is permitted, but republication/redistribution requires IEEE permission. See http://www.ieee.org/publications_standards/publications/rights/index.html for more information.

Authorized licensed use limited to: Texas A M University. Downloaded on August 08,2023 at 18:34:41 UTC from IEEE Xplore. Restrictions apply.

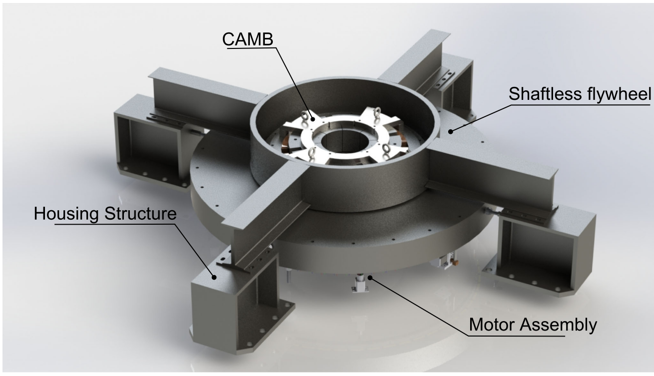

Fig. 1. SHFES flywheel with rated energy and power of 100 kWh/100 kW. The combination AMB is PM biased, Homopolar to provide 5-DOF levitation.

peak power output [11], [12] proposed a 100 KWh, 2 MW flywheel made of composite material. It has a specific energy of 15–18 Wh/kg. Active Power Inc. has developed a series of flywheels capable of 3 kWh and 675 kW for UPS application, and a single unit weighs 4976 kg.

The current FESSs have yet to be widely adopted as a utility-scale energy storage solution. They have a higher capital cost than electrochemical batteries [2], [13]. For instance, the Beacon Power's flywheel system costs more than ten times of a Li-on battery system with similar energy capacity even though it can provide a competitive cost/(kWh∗cycles) considering its higher charge/discharge cycles. Compared to other technologies like batteries or supercapacitors, FESSs have "moving" parts. Thus, they are considered to have higher uncertainties in failure modes. Composite flywheels are particularly subject to this shortcoming because of their higher operational speeds and the unpredictable mechanical property of the material. At last, the majority of the existing flywheel systems are designed for specific applications. They require specialized knowledge and techniques for manufacture, assembly and maintenance, preventing them from being produced en masse with a lower cost per unit.

Texas A&M University has developed a novel AMB-supported FESS that features a patented shaftless, hubless high-strength steel flywheel [14] with an energy capacity of 100 kWh, a power rating of 100 kW, and operation duration of 1 h. The system will be referred to as **s**haftless, **h**igh-strength steel **f**lywheel **e**nergy **s**torage system (SHFES) in the remainder of this paper. The goal of this project is to introduce an innovative and commercially viable utility-scale FES system for grid application.

II. Overview of the SHFES

The SHFES is an extension and physical realization of the concepts presented in [15] and [16] by the coauthors. This effort was originally supported in 2007 by the American Association of Railroads and later in 2011 by the U.S. Department of Energy through Calnetix Inc. Its design schematic is depicted in Fig. 1. Its main specifications are summarized in Table I. The shaftless flywheel is in the form of a solid disc. High-strength steel is adopted as the building material so that it can

TABLE I
Flywheel Specifications

Parameter Name	Quantity	Unit/Standard
Outer diameter/ Height	2133/203	mm
Mass	5443	kg
Moment of inertia	3087	kg·m^2
Rotational speed	5000	r/min
Tip speed	558	m/s
Energy/Power capacity	100/100	kWh/kW
Materials	4340	AISI
Material tensile strength	1500	MPa
Linear relative permeability	200	-

provide competitive power and energy capacity at a much lower cost. The fabrications, manufacture, and recycling are also made easy, with the composite component being replaced. Moreover, SHFES has predictable fatigue life cycles, which are designed to last for 30 years of operation. As shown in Fig. 1, the design of SHFES is entirely different from a conventional flywheel that has a shaft and hole through its center. The core component of the SHFES is a shaftless, hubless high-strength steel flywheel weighing 5443 kg, which is sandwiched between the AMB and the motor/generator system. On top of the flywheel lies a single combination AMB (CAMB) that is designed to provide 5-DOF magnetic suspension for the 5443 kg rotor. The CAMB is supported by a housing structure that is bolted to the ground. A catcher bearing is installed underneath the flywheel for drop protection. Spacers are placed between the CAMB and the flywheel in case of CAMB failure. For the custom coreless permanent-magnet (PM) motor/generator, its coils are installed on a movable holding structure. During charge/discharge, they will be inserted into the flywheel's motor slot. A six-step current-regulated voltage source inverter is used to drive the motor. To increase the efficiency, the flywheel is designed to work in a vacuum chamber.

In the remainder of this paper, the design and analysis of the shaftless and hubless flywheel are presented. The magnetic bearing's working principle and magnetic suspension control are also discussed. Motor design is presented as well. In the end, initial testing results of the first-of-its-kind SHFES are presented.

III. Design of the Shaftless Flywheel

The maximum kinetic energy that a flywheel can store is an outcome of both its moment of inertia (I) and maximum allowable spinning speed (ω)

$$E = \frac{1}{2} I \omega^2. \tag{1}$$

For energy capacities, flywheels are designed to have a higher moment of inertia and to rotate at a higher spinning speed. Since the stored energy is proportional to the square of the spinning speed, raising ω increases the storage energy dramatically. However, a very high spinning speed will eventually lead to failures caused by the stress developed by inertia loads. It was further investigated in [17] that the maximum specific energy (energy per mass, E_m) and the maximum energy density (energy per

Authorized licensed use limited to: Texas A M University. Downloaded on August 08,2023 at 18:34:41 UTC from IEEE Xplore. Restrictions apply.

volume, E_v) of a flywheel are determined by its shape factor (K) and the material's maximum strength ($\sigma_{\max}$)

$$\begin{aligned} E_v &= K\sigma_{\max} \\ E_m &= K\sigma_{\max}/\rho. \end{aligned} \tag{2}$$

The shape factor K is determined by the flywheel's geometric profile. For instance, a Laval disc [18] boasts an ideal shape factor of one. However, its geometry profile makes it very difficult to be manufactured or magnetically suspended. A conventional flywheel in the form of an annulus disc will have a shape factor of 0.3 or lower, depending on the ratio of the inner-to-outer radius and shrink-fit allowance. Meanwhile, the proposed shaftless flywheel has a shape factor close to 0.6. To take advantage of the shaftless design, high-strength steel (HSS) is chosen as the material. Composite materials are often chosen to make FESS flywheels for its low density and high tensile strength. They may have very high specific energy which is crucial in aerospace or mobile applications. However, ground-based, utility-scale FESS applications are much less reliant on system weight reduction but sensitive to the cost. HSS flywheels, on the other hand, have competitive energy density due to their high mass density and moderate yield strength, therefore are very suitable for fixed, ground-based, large capacity applications. Composite materials are also not magnetically permeable, making the shaftless design inapplicable. Furthermore, HSS flywheels are superior to composite ones in terms of thermal conductivity and reliability since they have more available design data such as Stress-Cycle (SN) curves and fracture toughness [14].

A. *Shaftless Flywheels Versus Annular Flywheels*

The conventional design of FESS includes a flywheel with a center borehole which will significantly increase the loop stress. To overcome this shortness, the presented SHFES is in the form of a solid disc to improve its energy density. In the following, the stress levels and energy densities of shaftless and annular flywheels are compared.

A rotating flywheel is subject to both hoop (σ_θ) and radial (σ_r) stress

$$\frac{d}{dr}(r\sigma_r) - \sigma_\theta + \rho\omega^2 r^2 = 0 \tag{3}$$

where ρ denotes the materials density and ω the spinning speed and r the radial position. The Von-Mises (σ_{vm}) yield criterion is usually used for flywheel designing

$$\sigma_v = \sqrt{\sigma_r^2 + \sigma_\theta^2 - \sigma_r\sigma_\theta}. \tag{4}$$

The maximum rotational velocity can be determined when the maximum Von-Mises stress for solid and annulus flywheel are close to material's yield strength (σ_y). For the latter case, the shrink-fit-induced stress (σ_{sh}) also needs to be considered

$$\begin{aligned} \sigma_{vm}\,(\text{shaftless}) &= \frac{3+v}{8}\rho\omega^2 b^2 \\ \sigma_{vm}\,(\text{annular}) &= \sigma_{sh} + \frac{1}{4}\left[(1-v)\,a^2 + (3+v)\,b^2\right]\left(\rho\omega^2\right) \end{aligned} \tag{5}$$

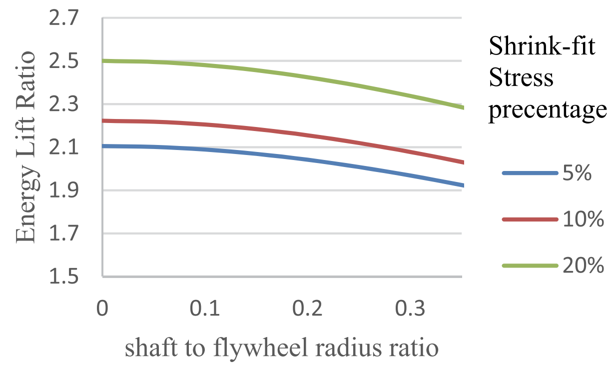

Fig. 2. Ratios of specific energy and energy density of shaft-less to annular flywheels. The horizontal axis is the ratio of shaft radius to flywheel radius. The different curves are results of stresses caused by different shrink-fit allowances. In general, the shaftless flywheel will have a doubled energy density.

where v denotes the Poisson's ratio, and a and b are the inner and outer radius, respectively. The maximum Von-Mises stress occurs at the inner radius of an annular disc. The maximum allowable spinning speeds derived from (5) is then applied to (1) for determining the maximum specific energy and energy density of shaftless and annular flywheel

$$\begin{aligned} \frac{E}{m}\,(\text{shaftless}) &= \frac{2\sigma_y}{\rho\,(3+v)} \\ \frac{E}{m}\,(\text{annular}) &= \frac{(\sigma_y - \sigma_{sh})\left(a^2+b^2\right)}{\rho\left[(1-v)\,a^2 + (3+v)\,b^2\right]}. \end{aligned} \tag{6}$$

By comparing these two results, the energy density lift ratio (λ_k) of the shaftless flywheel to an annular flywheel is defined as

$$\lambda_k = \frac{2}{(1-\Delta\sigma)}\left[1 - \frac{2\,(1+v)\,t^2}{(1+t^2)\,(3+v)}\right] \tag{7}$$

where $t = a/b$ denotes the ratio between the inner and outer radius (equivalent to shaft-to-flywheel radius) for the annular flywheel and $\Delta\sigma$ denotes the ratio of shrink-fit-caused stress to the material's yield stress. It can be concluded from Fig. 2 that a lift ratio of 2 is guaranteed for most cases where the shaft to flywheel radius ratio is small, making the proposed flywheel nearly double its specific energy to 18–21 Wh/kg and energy density to $138 - 161$ kWh/m^3. Composite flywheels reportedly [3]–[5] have similar or higher specific energy due to their low density and higher hoop tensile stress. However, they need to be operating at a much higher speed (typically above 10 000 r/min) to provide the same energy and have much higher cost for the materials and fabrication.

B. *Life Cycles, Costs, and Recycling*

The flywheel's life cycle depends on the ratio between the maximum and minimum stress it experiences in one cycle. This ratio (R) is dependent on the depth of discharge (DOD) based on the following equation [15]:

$$R = \sigma_{\min}/\sigma_{\max} = (1 - \text{DOD}). \tag{8}$$

Since the shaftless flywheel can store 117 kWh at the maximum speed, with a DOD of 85%, it has an energy capacity of

Authorized licensed use limited to: Texas A M University. Downloaded on August 08,2023 at 18:34:41 UTC from IEEE Xplore. Restrictions apply.

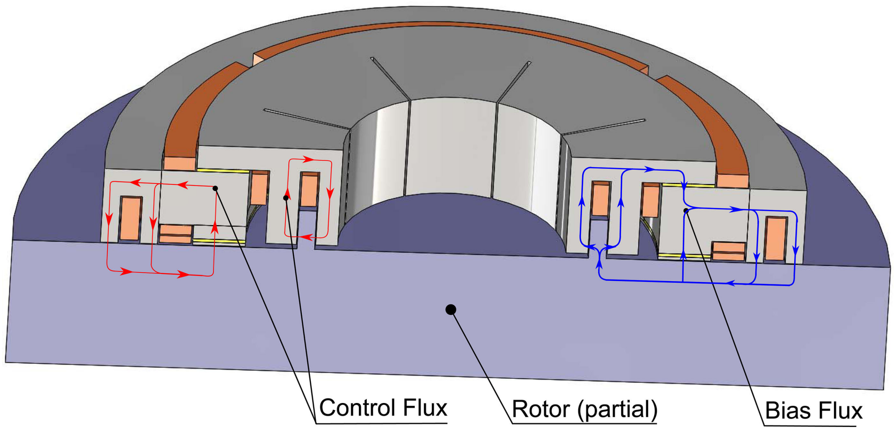

Fig. 3. Section view of the CAMB flywheel assembly. For better illustration purposes, the flywheel is truncated radially without affect the magnetic flux paths. For the same reason, the PM bias flux path is only highlighted in the right half of the section, and the EM flux paths are only highlighted in the left half. Note that there are eight radial control coils, four tilting control coils, and two axial control coils.

TABLE II
CAMB SPECIFICATIONS

Parameter Name	Quantity	Unit/Standard
Outer diameter/Height	1106/165	mm
Mass	544	kg
Materials	1010	AISI
Material tensile strength	350	MPa
Linear relative permeability	1000	-

100 kWh. The life cycle is derived from (9) according to [19]

$$\log(N_f) = 11.62 - 3.75\log(S - 80)$$
$$S = \sigma_{\max}(1 - R)^{0.44} \quad (9)$$

where N_f denotes the life cycles. With a DOD of 85%, the SHFES has 100 k life cycles, which is significantly higher than typical li-on batteries. Since the DOD is a scalable factor, the flywheel can operate at a lower DOD to give an even higher life cycle. For instance, a DOD of 60% (70 kWh) gives about 460 k. The cost of AISI 4340 steel is about \$1 to \$5 per kilogram. Composite flywheels are typically made of fiberglasses and carbon fibers, which cost about \$3–5 and \$20–30 per kilogram, respectively. The strength per unit cost of steel flywheel (1400 MPa/\$) is much higher than both of these materials (400 and 200 MPa/\$) [18], [20]. There are other unique advantages of HSS-based flywheel technology. Fatigue cracks will develop in the flywheel when it reaches the end of its life cycle. The SHFES can constantly be monitored by many existing noninvasive methods developed for monitoring steel structures such as ultrasound or acoustic-based methods, without interrupting the operation. Recycling of the SHFES only requires re-forging the flywheel. The other option is simply fixing the existing cracks and let the flywheel work at a lower revolutions per minute. To improve its performance, the shaftless flywheel is forged and machined as a single piece with the effort of eliminating cavities. In addition, balancing holes are machine around the outer radius so that they do not cause stress concentration when the flywheel is spinning.

IV. AMB AND LEVITATION CONTROL

A. Overview of the CAMB

Energy storage flywheels are typically supported by AMBs to avoid mechanical friction loss. A conventional FESS includes several magnetic bearings installed at different locations along the shaft for radial and axial levitation correspondingly. Typically, two sets of radial AMBs are responsible for controlling radial and tilting motion of the flywheel while thrust bearings are used solely for axial motion control. For the SHFES, a dedicated homo-polar combo-AMB system is introduced. The unique design provides 5-DOF levitation by a single AMB. Its half-section view is depicted in Fig. 3. The CAMB is PM biased. Both radial bias flux and axial bias flux are supplied by two PM rings that are bright yellow. The bias flux provides the majority of the electromagnetic force to counter the flywheel weight at the designed equilibrium position. They also make the AMB homo-polar, which reduces eddy current and hysteresis loss induced by the flywheel's rotation motion [21]. Furthermore, the PMs are used as high reluctance barriers between the radial and axial/tilting control flux paths. For radial control, a single pair of two radial poles is designed to have the same bias flux density so that the net radial force is zero when the flywheel is centered and when no radial excitation current is applied. However, flux circulation generated by the radial excitation current strengthens one of the radial poles and weakens the other one, resulting in a net radial force. The outer portion of the CAMB provides axial and moment control. There are four tilting coils in total and each can vary the flux in its own quadrant of the CAMB. Moment control is realized by giving an excitation current to one tilting coil and the same amount of current with opposite direction to the opposite tilting coil with respect to the moment axis so that no axial force is generated. For axial control, two large ring-shaped axial coils are installed for varying the flux strength throughout the entire axial flux path so that the axial force is provided without generating any moment.

The CAMB's dimensions and materials are refined by intensive nonlinear 3-D Finite Element Electromagnetic Analysis using commercial FEA software. It was found that low carbon

Authorized licensed use limited to: Texas A M University. Downloaded on August 08,2023 at 18:34:41 UTC from IEEE Xplore. Restrictions apply.

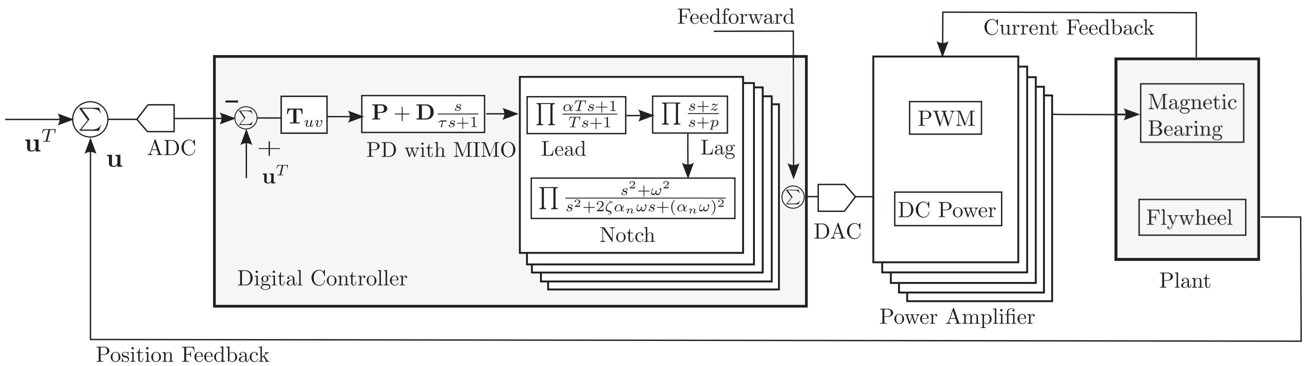

Fig. 4. Overall feedback control architecture, including a five-channel position and current loop. The position regulator is implemented in a dSPACE DS1103 digital controller. Each channel in the position regulator consists of multiple lead/lag compensators and notch filters and a feedforward component.

steels with proper heat treatments will result in satisfying saturation flux density (B_s) and relative permeability (μ_r). With a sufficient magnetic property, it also beats electrical steels in price and availability. Apart from its magnetic properties, the AMB is also designed to have a lower weight in the effort of increasing the stator structure's stiffness to facilitate the controller design. Although low frequency modes from the stator structure can be compensated by derivative feedback in the controller, it is preferable to use a low derivative gain, for a high derivative gain will in return magnify high frequency resonances.

B. Control of the CAMB

As depicted in Fig. 4, the AMB's control system includes position feedback regulators and current feedback regulators. The position feedback signals are acquired by proximity sensors in the form of voltages (10). The sensor bandwidths are over 10 kHz

$$\mathbf{u} = \begin{bmatrix} V_{rx+} & V_{rx-} & V_{ry+} & V_{ry-} & V_{zy+} & V_{zy-} & V_{zx+} & V_{zx-} \end{bmatrix}^T. \tag{10}$$

The position reference signals use the sensor's coordinate so that the targets can be conveniently recorded by manually adjusting the flywheel's position to compensate for the AMB's installation inaccuracy. A coordinate transformation (11) is then performed to convert the error signals to the AMB actuator's coordinate in (12)

$$\mathbf{T}_{uv} = \begin{bmatrix} \frac{1}{2} & \frac{1}{2} & 0 & 0 & 0 & 0 & 0 & 0 \\ 0 & 0 & \frac{1}{2} & \frac{1}{2} & 0 & 0 & 0 & 0 \\ 0 & 0 & 0 & 0 & \frac{1}{2R} & \frac{-1}{2R} & 0 & 0 \\ 0 & 0 & 0 & 0 & 0 & \frac{-1}{2R} & \frac{1}{2R} & 0 \\ 0 & 0 & 0 & 0 & \frac{1}{4} & \frac{1}{4} & \frac{1}{4} & \frac{1}{4} \end{bmatrix} \tag{11}$$

$$\mathbf{v} = \begin{bmatrix} V_x & V_y & V_{\theta x} & V_{\theta y} & V_z \end{bmatrix}^T. \tag{12}$$

There are more sophisticated adaptive control methods for AMB such as sliding modes and H-infinity, but the position controller adopted in this project is based on the proportional–derivative (PD) control, which is easily implemented. The integrator is replaced by lag compensators to eliminate the possibility of integral wind-up. A decoupled five-channel PD controller can provide stable control for the flywheel at low speed. However, under higher speed, the flywheel system is subject to the gyroscopic effect characterized by pairs of forward and backward whirling modes that are speed dependent. For instance, the rigid body backward and forward modes converge to 0 and $(I_p/I_t)\omega$, respectively, as the spin speed increases. Since the shaftless flywheel has a substantial diameter-to-height ratio, it also has a very large ratio of the primary-to-transversal moment of inertia, which amplifies the gyroscopic effect. Increasing derivative gain in a single-input-single-output (SISO) controller provides little phase lead for the low-frequency backward mode and may cause bus voltage saturation problems for the high-frequency forward mode. Therefore, as defined in (13), an extra multiple-input-multiple-output (MIMO) control stage is included in the PD controller

$$\mathbf{P} = \begin{bmatrix} Px & 0 & 0 & 0 & 0 \\ 0 & Py & 0 & 0 & 0 \\ 0 & 0 & P_{\theta x} & -P_{\theta c} & 0 \\ 0 & 0 & P_{\theta c} & P_{\theta y} & 0 \\ 0 & 0 & 0 & 0 & P_z \end{bmatrix} \quad \mathbf{D} = \begin{bmatrix} Dx & 0 & 0 & 0 & 0 \\ 0 & Dy & 0 & 0 & 0 \\ 0 & 0 & D_{\theta x} & D_{\theta c} & 0 \\ 0 & 0 & -D_{\theta c} & D_{\theta y} & 0 \\ 0 & 0 & 0 & 0 & D_z \end{bmatrix} \tag{13}$$

where $P_{\theta c}$ and $D_{\theta c}$ are the cross-couple proportional and damping coefficients. In the effort of weakening the gyroscopic effect, the cross-coupled feedback in (13) applies torque in one plane per the angular position and velocity in its quadrature plane. This strategy reduces the speed dependency of the system dynamics (conical modes) and lowers the frequency of forward modes so that derivate gain can be more effective [22]. In addition to the PD regulators and lag compensators, each feedback channel also includes various lead compensators and notch filters. The lead compensators provide finite bandwidth gain for a specific frequency range so that the system's stability or response can be improved. The transfer function being used for the lead compensator is defined in

$$\prod_i \frac{\alpha_i T_i s + 1}{T_i s + 1}, \quad \text{where } \alpha_i = \frac{1 + \sin(\phi_i)}{1 - \sin(\phi_i)}, \qquad T_i = \frac{1}{\omega_i(c)\sqrt{\alpha_i}} \tag{14}$$

Authorized licensed use limited to: Texas A M University. Downloaded on August 08,2023 at 18:34:41 UTC from IEEE Xplore. Restrictions apply.

in which ϕ_i and $\omega_i(c)$ denote the maximum phase and the center frequency, respectively. The notch filters are critical in suppressing synchronous vibration caused by imbalance forces when the rotor passes critical speeds during speed-up or coast-down. They are also instrumental in canceling high-frequency structural modes or suppressing sensor runouts that would be amplified by derivative feedback. The sensor runouts could lead to amplifier saturations and instabilities if left unattended. The transfer functions of notch filters are given by the following equation:

$$\prod_i \frac{s^2 + \omega_i{}^2(n)}{s^2 + 2\zeta_i\beta_i\omega_i(n)s + (\beta_i\omega_i(n))^2} \tag{15}$$

where ζ_i determines the rejection bandwidth and depth. $\omega_i(n)$ is the notch frequency and β_i decides the pole position offset. The PD regulators, lead/lag compensators and notch filters are programmed in an embedded digital controller (dSPACE DS1103), which is working at 50 μs. For each channel, three notch filters, three lead compensators, and one lag compensator are implemented. The SHFES utilizes single phase commercial power amplifiers that are working in the current mode. The nominal dc-bus voltage is 160 V, and the switching frequency is 15 Khz.

C. Closed-Loop Dynamic Model

The equation of motion for the AMB-supported rotor is summarized in (16), shown below. The first equation presents the dynamics of the stator. The second is for the dynamics of the flywheel (rotor), and the last equation describes the magnetic force and controller

$$\begin{cases} \mathbf{M}_s\ddot{\mathbf{q}}_s + \mathbf{C}_s\dot{\mathbf{q}}_s + \mathbf{K}_s\mathbf{q}_s = -\mathbf{f}_m \\ \mathbf{M}_r\ddot{\mathbf{q}}_r + (\mathbf{C}_r + \omega\mathbf{G}_s)\dot{\mathbf{q}}_r + \mathbf{K}_r\mathbf{q}_r = \mathbf{f}_m \\ \mathbf{f}_m = \mathbf{K}_p(\mathbf{q}_s - \mathbf{q}_r) + \mathbf{K}_i\mathbf{G}_p\mathbf{TF}_c\mathbf{G}_s(\mathbf{q}_s - \mathbf{q}_r + \mathbf{q}_t) \end{cases} \tag{16}$$

where $[\mathbf{q}_s, \mathbf{q}_r, \mathbf{q}_t]^T$ denotes the stator position, the rotor position, and the target vectors, respectively. $\mathbf{M}_s$, $\mathbf{C}_s$, $\mathbf{K}_s$ and $\mathbf{M}_r$, $\mathbf{C}_r$, $\mathbf{K}_r$ denote the mechanical mass, damping, and stiffness matrices of the stator and rotor, respectively. $\mathbf{G}_r$ denotes the gyroscopic matrix. $\mathbf{K}_p$ and $\mathbf{K}_\mathrm{i}$ are the position and current stiffness matrices of the AMB. The current stiffnesses are frequency-dependent due to the eddy current effects. Their magnitudes decrease and phase lags increase as the frequency increases. $\mathbf{TF}_c$ is the controller's transfer function matrices. $\mathbf{G}_p$ and $\mathbf{G}_s$ are the transfer function matrices of the power amplifiers and proximity sensors, respectively. $\mathbf{G}_p$ is a simplified first-order servo-amplifier model, including nonlinearities such as voltage and current saturations [20]. The coordinate transformation has no effect on dynamics and, therefore, is ignored in the model. Motor dynamics are not included in this model either since it has minimal effects on magnetic suspension. The flywheel is assumed to be ideally speed controlled by the BLDC motor. To demonstrate the MIMO controller's effectiveness, Fig. 5 shows simulation results of the flywheel operating at high speed without MIMO control at first. The flywheel is experiencing significant vibrations in the θ_x–θ_y plane and the power amplifier voltage outputs oscillate between saturation values.

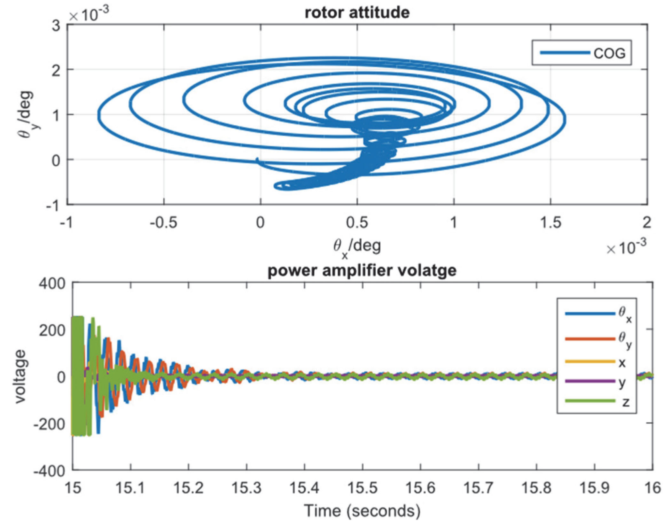

Fig. 5. Simulation results of flywheel vibration and amplifier voltage with MIMO controller switched on after 15 s.

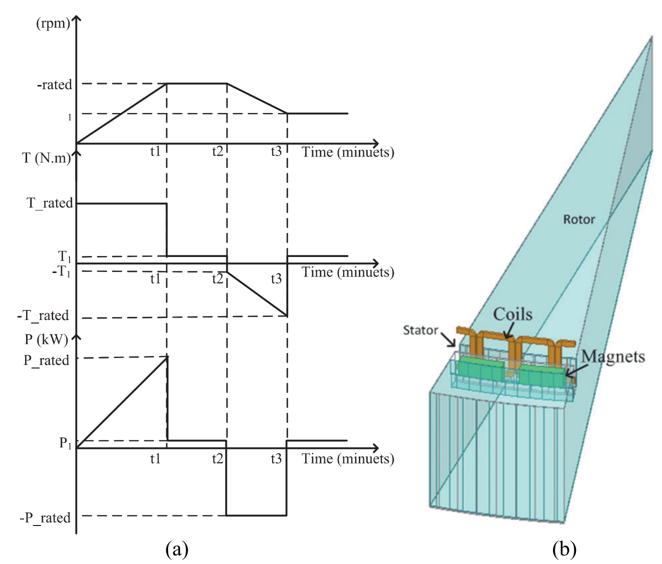

Fig. 6. (a) Motor/generator design requirement. (b) Motor/generator structure section view. The flywheel and motor are displayed upside down for illustration purposes.

After the MIMO controller is engaged, the flywheel stabilizes and amplifier saturations are alleviated.

V. Motor Design

The motor/generator designed for the flywheel is a coreless PM machine. The coreless windings are fixed on a movable base placed on the ground through holding structures. This design allows higher strength and reliability compared to the existing holding structures for coreless machines.

The flywheel's rated speed (ω rated), rated torque (T rated), and rated power (P rated) are 523 rad/s (5000 r/min), 191 N·m, and 100 kW, respectively. The design requirements for the power, speed, and torque are illustrated in Fig. 6(a). During 0 to t_1, the flywheel is charged with a constant torque to ω rated. During t_1 and t_2, the flywheel maintains the rated speed with

Authorized licensed use limited to: Texas A M University. Downloaded on August 08,2023 at 18:34:41 UTC from IEEE Xplore. Restrictions apply.

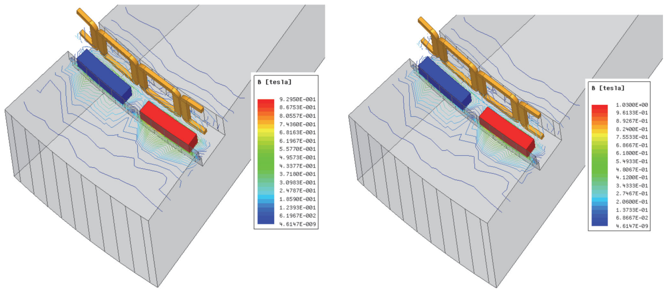

(a) (b)

Fig. 7. Motor/generator flux plot. (a) PM motor/generator flux density distribution by magnets and stator current: 210 A. (b) PM motor/generator flux density distribution by magnets and stator current: 300 A.

TABLE III
MOTOR/GENERATOR SPECIFICATIONS

Parameter Name	Quantity	Unit/Standard
Outer rotor diameter	2133	mm
Air-gap/groove stack height	50	mm
Motor/generator stack length	50	mm
Magnet height	25	mm
Number of poles/magnets	64	–
Number of phases	3	–
Magnet type	NdFe48	–
Number of turns for each coil	40	–
Air-gap/groove outer diameter	1904	mm
Air-gap/groove inner diameter	114	mm
Winding height	50	mm
Magnet thickness	15.54	mm
Number of slots	96	–
Magnet embrace	0.72	–
Winding type	Concentric	–
Number of parallel paths for each phase	32	–
Motor/generator drive specification		
DC-bus voltage	600	V
Maximum current	750	A
Switching frequency	16	kHz

minimum power consumptions. The flywheel operates in the generating mode between t_2 and t_3, during which it discharges at a constant power while its speed decreases from the rated value down to 201.8 rad/s (1928 r/min). Per the design requirement, t_1 and t_3-t_2 are 140 and 60 min, respectively. The standby duration t_2 is entirely based on the application. Fig. 6(b) depicts a section view of the proposed PM motor/generator with only two poles. Note that the view is upside down for a better illustration. During the operation, windings are placed inside the flywheel's motor groove, which has a depth of 50 mm and a width of 46.5 mm. In consideration of centrifugal forces, magnets (25 mm in height and 15.54 mm width) are mounted on the inner surface of the groove. The PM machine has 96 coils and 64 poles in total.

The specifications of the motor/generator are given in Table III. During the constant torque mode, the current stays at 210 A while the output power increases with speed. On the contrary, during the constant power mode when the rotor speed decreases, the current increases to maintain the same power output. Fig. 7(a) illustrates the flux plot when the magnets are magnetized and the stator carries its rated current at the rated speed. The maximum flux density is 0.92 T. Fig. 7(b) exemplifies the flux plot at 1928 r/min. In this case, the flux density increases moderately due to the increased coil current of 300 A. As it is represented in the two given flux plots, flux paths close themselves mostly in the air around the magnets and coils. It is owing to the use of less permeable steel-4340 as the rotor material to have a higher mechanical strength. Further details of design procedure and performance of the PM motor/generator are presented in [23].

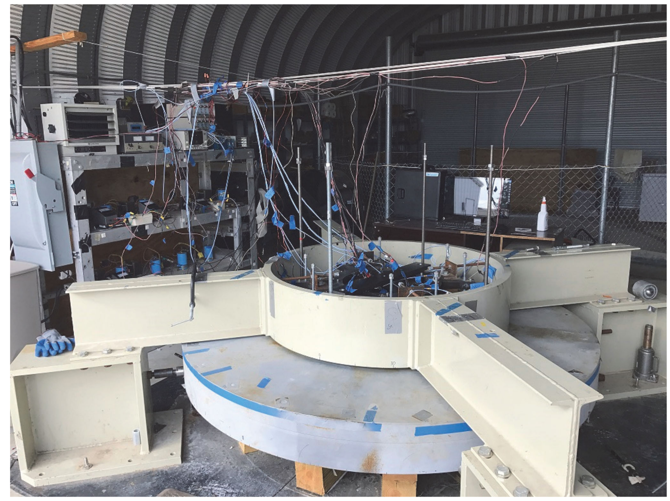

Fig. 8. SHFES during testing.

VI. INITIAL TEST

A small-scale, 90 kg SHFES was built and tested in 2014 [14]. Based on it, a refined full-scale, proof-of-concept SHFES with a 5443-kg flywheel (shown in Fig. 8) is then built at a dedicated testing facility that includes a 3-m (10 ft.) deep pit. The pit is lined with a soil retainer wall, which would be readily penetrated in the event of a flywheel burst, allowing the surrounding soil to capture the energy in a relatively harmless manner. In addition, the retainer wall also serves as the vacuum enclosure. During initial testing, the flywheel is not placed in the pit for better accessibility.

A. Radial and Axial Levitation

Based on the system dynamics simulation implemented in MATLAB/Simulink, the control parameters are derived and then fine-tuned during the onsite testing at the facility. Two lead compensators at 5 and 2 Hz are activated for each radial axis, which has less problem during lift-up due to their comparably few coil inductances. For the axial and tilt coils, one lead compensator at 10 Hz and two notch filters at 232 and 383 Hz are used. These two resonance frequencies are correspondent to the first and second bending modes of the flywheel.

The levitation test is carried out in two steps: At first, the flywheel is radially controlled while it is still vertically supported by the ball transfers. This technique facilitates the axial levitation later because that the CAMB's axial magnetic flux

Authorized licensed use limited to: Texas A M University. Downloaded on August 08,2023 at 18:34:41 UTC from IEEE Xplore. Restrictions apply.

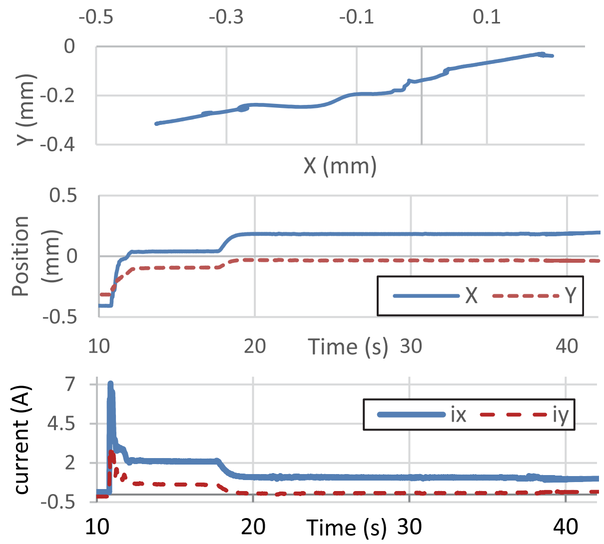

Fig. 9. Measurement of position and current signals during radial levitation. The radial targets are set per the CAMB's geometric center rather than the magnetic center.

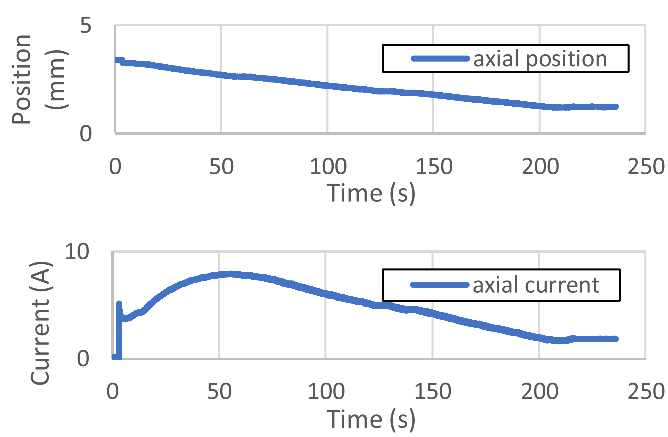

Fig. 10. Measurement of position and current signals during axial levitation. The target signal is gradually moved to 1.25 mm.

distribution also relies on its radial position. As depicted in Fig. 9, the flywheel is at first controlled radially to move from its initial position (-0.42 mm, -0.31 mm) to an intermediate position at (0.04 mm, -0.09 mm) before it finally reaches the geometric center (0.19 mm, -0.04 mm). Fig. 9 shows that there are steady-state current excitations when the flywheel reaches its radial center. These currents are compensating the inevitable manufactural and assembling inaccuracies, which causes the flywheel to experience PM pulling force at its geometric center. The gravity force may contribute in the radial directions as well since the flywheel is not perfectly leveled. Once the flywheel reaches its radial targets, the axial control is then switched on and the axial command is gradually raised to the target value of 1.25 mm to prevent de-levitation resulted by a large overshoot. As illustrated in Fig. 10, the axial control current goes up to 8 A to lift the flywheel at the starting air gap of 3.41 mm. Once it is off the ball transfers, the control current begins to drop gradually as the flywheel approaches its target. At the steady state, the air gap between the flywheel and the AMB is about 0.2 mm larger than the magnetic equilibrium point (1.05 mm). The flywheel is set to stay slightly below the neutral position to prevent it from jumping and damaging the AMB in case of power shortage. As a result, there is about 1.87 A of steady-state axial current for providing partial lifting force while the majority of the flywheel's weight is suspended by the PM-generated pulling force. The tilting coils are used for merely maintaining the flywheel's leveled orientation during the axial levitation.

VII. Conclusion and Future Work

The SHFES introduced in this paper is aimed at providing a more commercially viable flywheel energy storage technology for utility applications. In addition to the innovative shaftless flywheel and CAMB design that yields high energy and power capacity. The SHFES also utilizes low-cost and readily available high-strength steels as the building materials, making it a considerate advancement of the state-of-art flywheel technology.

The next step is the motor/generator installation and high-speed test. To demonstrate its performance, the SHFES will be tested with variable electrical loads and renewable energy resources under charging/discharging modes. Other future works include: To further reduce the costs of SHFES, the prototype system has a relatively high-cost and CPU-based controller. Because of that the nature of the AMB and the motor controls require multichannel feedbacks. Field programmable gate arrays (FPGA) can provide a cost-effective and high-performance controller solution for the both of them [24]. In addition, an in-depth study of the shaftless flywheel's failure modes is needed so that the safety design could be improved to meet commercial standards.

References

[1] B. P. Roberts and C. Sandberg, "The role of energy storage in development of smart grids," *Proc. IEEE*, vol. 99, no. 6, pp. 1139–1144, Jun. 2011.

[2] J. S. Remillard, "Facility scale energy storage: Applications, technologies, and barriers," *Strateg. Plan. Energy Environ.*, vol. 36, no. 2, pp. 22–42, 2016.

[3] R. Sebastián and R. Peña Alzola, "Flywheel energy storage systems: Review and simulation for an isolated wind power system," *Renew. Sustain. Energy Rev.*, vol. 16, no. 9, pp. 6803–6813, 2012.

[4] K. Veszprémi and I. Schmidt, "Flywheel energy storage drive for wind turbines," in *Proc. 7th Int. Conf. Power Electron. Drive Syst.*, 2007, pp. 916–923.

[5] S. M. Mousavi, G. F. Faraji, A. Majazi, and K. Al-Haddad, "A comprehensive review of flywheel energy storage system technology," *Renew. Sustain. Energy Rev.*, vol. 67, pp. 477–490, 2017.

[6] J. Abrahamsson, M. Hedlund, T. Kamf, and H. Bernhoff, "High-speed kinetic energy buffer: Optimization of composite shell and magnetic bearings," *IEEE Trans. Ind. Electron.*, vol. 61, no. 6, pp. 3012–3021, Jun. 2014.

[7] P. Tsao, "An integrated flywheel energy storage system with homopolar inductor motor/generator and high-frequency drive," Ph.D. dissertation, Dept. Elect. Eng. Comput. Sci., Univ. Calif., Berkeley, CA, USA, 2003.

[8] A. Kailasan, T. Dimond, P. Allaire, and D. Sheffler, "Design and analysis of a unique flywheel energy storage system—An integrated flywheel, motor/generator and magnetic bearing configuration," *J. Eng. Gas Turbines Power*, vol. 137, no. April, pp. 1–12, 2015.

[9] A. C. Arvin and C. E. Bakis, "Optimal design of press-fitted filament wound composite flywheel rotors," *Compos. Struct.*, vol. 72, no. 1, pp. 47–57, 2006.

[10] T. H. Sung, J. S. Lee, Y. H. Han, S. C. Han, S. K. Choi, and S. J. Kim, "300 Wh class superconductor flywheel energy storage system with a horizontal axle," *Phys. C Supercond. Appl.*, vol. 372–376, part 3, pp. 1451–1456, 2002.

Authorized licensed use limited to: Texas A M University. Downloaded on August 08,2023 at 18:34:41 UTC from IEEE Xplore. Restrictions apply.

[11] Beacon Power, "20 MW Flywheel energy storage plant," Tech. Memo, 2014. [Online]. Available: http://www.sandia.gov/ess/docs/pr_conferences/2014/Thursday/Session7/02_Areseneaux_Jim_20MW_Flywheel_Energy_Storage_Plant_140918.pdf

[12] R. F. Thelen, J. D. Herbst, and M. T. Caprio, "A 2 MW flywheel for hybrid locomotive power," in *Proc. IEEE 58th Veh. Technol. Conf.*, 2003, vol. 5, pp. 3231–3235.

[13] P. J. Janse Van Rensburg, A. A. Groenwold, and D. W. Wood, "Optimization of cylindrical composite flywheel rotors for energy storage," *Struct. Multidiscip. Optim.*, vol. 47, no. 1, pp. 135–147, 2013.

[14] X. Li, A. Palazzolo, P. McMullen, Z. Wang, and D. Tingey, "Shaft-less energy storage flywheel," in *Proc. ASME 9th Int. Conf. Energy Sustain.*, 2015, vol. 2, pp. 1–6.

[15] Z. Wang, "A novel flywheel and operation approach for energy recovery," Ph.D. dissertation, Dept. Mech. Eng., Texas A&M Univ., College Station, TX, USA, Dec. 2011.

[16] A. Palazzolo, Z. Wang, and R. Tucker, "Shaft-less energy storage flywheel," U.S. Patent 8 633 625, Jan. 21, 2014.

[17] G. Genta, *Kinetic Energy Storage: Theory and Practice of Advanced Flywheel Systems*. Waltham, MA: Butterworth-Heinemann, 1985.

[18] B. Bolund, H. Bernhoff, and M. Leijon, "Flywheel energy and power storage systems," *Renew. Sustain. Energy Rev.*, vol. 11, no. 2, pp. 235–258, Feb. 2007.

[19] U.S. Dept. Defense, "Metallic materials and elements for aerospace vehicle structures," Millitary Handbook-MIL-HDBK-5H, 1998.

[20] S. Sanders, M. Senesky, M. He, and L. Ten Hope, "Low-Cost flywheel energy storage demonstration," Calif. Energy Commission, Tech. Memo. CEC-500-2015-089, Jun. 2015. [Online]. Available: http://www.energy.ca.gov/2015publications/CEC-500-2015-089/CEC-500-2015-089.pdf

[21] M. E. F. Kasarda and P. E. Allaire, "Comparison of predicted and measured rotor losses in planar radial magnetic bearings," *Tribol. Trans.*, vol. 40, no. 2, pp. 219–226, 1997.

[22] J. Park, A. Palazzolo, and R. Beach, "MIMO active vibration control of magnetically suspended flywheels for satellite IPAC Service," *J. Dyn. Syst. Meas. Control*, vol. 130, no. 4, p. 41005, 2008.

[23] B. Anvari, X. Li, H. A. Toliyat, A. Palazzolo, Z. Wang, and X. Han, "A coreless permanent-magnet machine for a magnetically levitated shaft-less flywheel," in *Proc. IEEE Int. Electric Mach. Drives Conf.*, 2017, pp. 1–7.

[24] E. Monmasson and M. N. Cirstea, "FPGA design methodology for industrial control systems—A review," *IEEE Trans. Ind. Electron.*, vol. 54, no. 4, pp. 1824–1842, Aug. 2007.

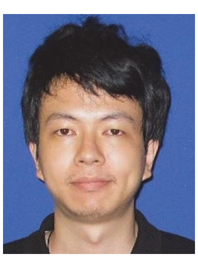

Xiaojun Li (S'17) received the M.S. degree in robotics from South China University of Technology, Guangzhou, China. He is currently working toward the Ph.D. degree in mechanical engineering at Texas A&M University, College Station, TX, USA.

He is currently involved in energy storage systems and MAGLEVs. Since January 2017, he has been with the Motion Control Group, Rockwell Automation, Milwaukee, WI, USA. His current research interests include kinetic/flywheel energy storage, magnetic levitation, embedded control systems, and artificial intelligence.

Bahareh Anvari (M'17) received the M.S. degree in electrical engineering from Shahid Beheshti University, Tehran, Iran, in 2013. She is currently working toward the Ph.D. degree in electrical engineering at Texas A&M University, College Station, TX, USA.

She is currently with the Advanced Electric Machines and Power Electronics Laboratory, Texas A&M University. Her current research interests include permanent-magnet machine design, switched reluctance machine design, and motor drives.

Alan Palazzolo received the M.S. and Ph.D. degrees in mechanical engineering from the University of Virginia, Charlottesville, VA, USA, in 1977 and 1981, respectively.

He is currently with Texas A&M University, College Station, TX, USA. He is an Endowed Professor. His current research interests include centrifuge-enabled desalination, flash-heated direct fuel injectors, heart pumps, rotating machinery vibrations, and VFD motor-related vibration modeling. He has authored or coauthored 80+ archival journal articles and is the author of the textbook *Vibration Theory and Applications with Finite Elements and Active Vibration Control*.

Prof. Palazzolo has received Best Paper awards from the *ASME Journal of Tribology*, a lifetime achievement award in magnetic bearings, and an R&D 100 award for ultra-high-temperature magnetic bearings

Zhiyang Wang received the M.S. degree in robotics from Harbin Institute of Technology, Harbin, China, and the Ph.D. degree in mechanical engineering from Texas A&M University, College Station, TX, USA.

He is currently the Principal Engineer in Calnetix/Upwing, Cerritos, CA, USA. He is in charge of magnetic bearings, rotordynamics, and motor design. He was a Lead Motor Engineer in FMC Technologies and a Senior Magnetic Bearing Engineer in GE Energy. He holds multiple patents on shaftless flywheel and magnetic bearings.

Hamid Toliyat (F'08) received the B.S. degree from Sharif University of Technology, Tehran, Iran, in 1982; the M.S. degree from West Virginia University, Morgantown, WV, USA, in 1986; and the Ph.D. degree from the University of Wisconsin-Madison, Madison, WI, USA, in 1991, all in electrical engineering.

He joined the Faculty of Ferdowsi University of Mashhad, Mashhad, Iran, as an Assistant Professor of Electrical Engineering. In March 1994, he joined the Department of Electrical and Computer Engineering, Texas A&M University, College Station, TX, USA, where he is currently a Raytheon Endowed Professor of Electrical Engineering. His work is highly cited by his colleagues (more than 17 000 times).

Dr. Toliyat received the prestigious Nikola Tesla Field Award for "outstanding contributions to the design, analysis, and control of fault-tolerant multiphase electric machines" from the IEEE in 2014. He was the Chair of the IEEE-IAS Industrial Power Conversion Systems Department of IEEE-IAS.

Authorized licensed use limited to: Texas A M University. Downloaded on August 08,2023 at 18:34:41 UTC from IEEE Xplore. Restrictions apply.